JOURNAL OF SPACECRAFT AND ROCKETS
Vol. 42, No. 1, January–February 2005

Jet Interaction in Supersonic Flow with a Downstream Surface Ramp

Y. H. Byun* and K. J. Bae†
Konkuk University, Seoul 143-701, Republic of Korea
S. Wallis,‡ V. Viti,§ and J. A. Schetz¶
Virginia Polytechnic Institute and State University, Blacksburg, Virginia 24060
and
R. Bowersox**
Texas A&M University, College Station, Texas 77843

An experimental and computational study has been performed for investigation of jet interaction in supersonic flow with a three-dimensional surface ramp located behind a sonic, transverse jet. The goal was to reduce the low-pressure region behind the jet, which produces an unwanted nose-down moment on a vehicle. The experimental techniques include conventional pressure taps, schlieren photos, and pressure-sensitive paint (PSP). The numerical solver used in this study is AeroSoft's structured flow solver GASP Version 4.0. A Mach 4 crossflow with a jet stagnation pressure ratio of 532 was considered, and the three-dimensional downstream ramp was designed by a parametric study using GASP. The computational-fluid-dynamics and PSP results are verified with pressure tap results, and all results are compared between the jet-only case and jet-plus-ramp case. The results showed that the ramp located downstream of the jet decreases the nose-down pitching moment without a net force loss.

Nomenclature

C_F	=	force coefficient
C_M	=	moment coefficient
C_p	=	pressure coefficient
I	=	luminescence intensity
k	=	turbulent kinetic energy, m^2/s^2
Ma	=	Mach number
P	=	static pressure, Pa
P_0	=	total pressure, Pa
T	=	static temperature, K
t	=	time, s
U	=	mean streamwise and scaled velocity, m/s
u, v, w	=	Cartesian velocity components, m/s
x, y, z	=	Cartesian coordinates, m
δ	=	boundary-layer thickness, m
ε	=	turbulence dissipation rate, m^2/s^2
μ	=	laminar (molecular) viscosity (first bulk viscosity coefficient), Ns/m^2
μ_T	=	turbulent (eddy) viscosity, Ns/m^2
ν	=	kinematic viscosity, m^2/s
ρ	=	density, kg/m^3
τ	=	shear stress, N/m^2
ω	=	turbulent frequency, m^3/s^3

Subscripts

e	=	values on the edge of the boundary layer
J	=	jet condition
ref	=	reference value

Superscripts

$\sim$	=	mean value of Favre-averaged variable
-	=	time-averaged values
$''$	=	fluctuating value of Favre-averaged variable
$*$	=	nondimensional value

Presented as Paper 2003-3933 at the AIAA 21st Applied Aerodynamics Conference, Orlando, FL, 23–26 June 2003; received 22 July 2003; revision received 16 February 2004; accepted for publication 16 February 2004.

*Professor, Department of Aerospace Engineering. Senior Member AIAA.
†Graduate Research Assistant; currently Researcher, Hanwha Corporation, Incheon 405-310, Republic of Korea. Member AIAA.
‡Graduate Research Assistant; currently Engineer, Dynetics, Inc., Crystal City, VA 22202. Member AIAA.
§Graduate Research Assistant; currently Postdoctoral Researcher, Department of Mechanical Engineering, University of Kentucky, Lexington, KY 40506. Member AIAA.
¶Fred D. Durham Chair, Department of Aerospace Engineering. Fellow AIAA.
**Associate Professor, Department of Aerospace Engineering. Associate Fellow AIAA.

Introduction

CONVENTIONAL methods of improving the aerodynamic control maneuver for high-speed vehicles are limited by the weight and drag requirements of the overall vehicle. Side jets can be ideal for enhancing the high-angle-of-attack performance of such an advanced concept because of their rapid response time as well as their ability to perform over a wide range of speeds and altitudes. Side jets have been recognized as an effective means for maneuvering and controlling vehicles, missiles, and projectiles since the mid-1960s.

When a jet is injected into the supersonic or hypersonic freestream, a number of complex fluid structures are generated. A region of separated flow is created by the pressure rise as the crossflow stagnates at the front of the jet, and a low-pressure, separated region forms in the jet wake. Shock waves are also present in the form of a barrel shock and a Mach disk in the plume of the jet and separation and bow shocks upstream of the jet. The far field of the jet is dominated by a counter-rotating vortex pair created in its wake, which is carried along just beneath the jet plume and retains its strength even as the jet itself dissipates. The surface pressure induced by this interaction leads to an increase in the direct force control. However, a generally unwanted nose-down moment is also produced. Some method for counteracting this nose-down moment must be introduced, leading to increased complexity and weight.

The aeroramp fuel injector as devised by Schetz and his coworkers at Virginia Polytechnic Institute and State University (Virginia Tech)[1] demonstrated high-pressure region increases and low-pressure region decreases in the region of jet interaction. An innovative idea using the concept of the aeroramp to enhance the performance of jet interaction control systems has been studied at Virginia Tech by applying secondary jets downstream of the main jet.[2] This did succeed in reducing the nose-down pitching moment dramatically, but this secondary jet system needs a more complex subsystem of gas supply and regulation.

In the current study, the effect of a ramp located downstream of the jet was examined experimentally and numerically. The goal was again to reduce the low-pressure region behind the jet, thus reducing the nose-down pitching moment, while minimizing any change in the net force. Tests were conducted at Mach 4.0 in the Virginia Tech Supersonic Wind Tunnel with a sonic jet at a stagnation pressure ratio of 532, and pressure-sensitive paint (PSP) was used for measurement of the surface-pressure field for quantitative analysis and schlieren photos were taken for qualitative analysis.

The advantage of the ramp is to make the mechanism simpler than the secondary injection arrangement, and some cases might use projecting parts, which are installed on the missile already. One can also envision using various surface shape change devices, which need only be employed when the side jet is active.

Description of the Computations

Equations and Solver

The flow of a viscous, heat-conducting, compressible, single-species, nonreacting fluid can be described using conservation of mass, conservation of momentum, and conservation of energy, generally known as the Navier–Stokes equations. For turbulent flows these equations can be written using time-averaged (Reynolds-averaged, indicated by an overbar) values of the density and pressure and mass-weighted (Favre-averaged, indicated by a tilde) averages for the velocity components and temperature. The Reynolds-averaged Navier–Stokes (RANS) form of the conservation of momentum equation, includes the Reynolds-stress tensor defined as

$$\tau_{ij} = -\bar{\rho}\widetilde{u_i'' u_j''} \tag{1}$$

In computational fluid dynamics (CFD) the Reynolds-stress tensor is simulated using a combination of assumptions and physical relations (first-order models) or it is directly resolved into its six components (second-order models). First-order models, also known as turbulent viscosity models, make use of the Boussinesq assumption

$$-\bar{\rho}\widetilde{u_i'' u_j''} = \mu_T\left(\frac{\partial \tilde{u}_i}{\partial x_j} + \frac{\partial \tilde{u}_i}{\partial x_j} - \frac{2}{3}\delta_{ij}\frac{\partial \tilde{u}_k}{\partial x_k}\right) - \frac{2}{3}\delta_{ij}\bar{\rho}k \tag{2}$$

All of the numerical calculations performed in this study used Wilcox's k–ω (1988) turbulence model.[3]

Eddy viscosity:

$$\mu_T = C_\mu(\bar{\rho}k/\omega) \tag{3}$$

Turbulent kinetic energy:

$$\rho\frac{\partial k}{\partial t} + \rho U_j\frac{\partial k}{\partial x_j} = \tau_{ij}\frac{\partial U_i}{\partial x_j} - \beta^*\rho k\omega + \frac{\partial}{\partial x_j}\left[\left(\mu + \sigma^*\mu_T\right)\frac{\partial k}{\partial x_j}\right] \tag{4}$$

Specific dissipation rate:

$$\rho\frac{\partial \omega}{\partial t} + \rho U_j\frac{\partial \omega}{\partial x_j} = \alpha\frac{\omega}{k}\tau_{ij}\frac{\partial U_i}{\partial x_j} - \beta\rho\omega^2 + \frac{\partial}{\partial x_j}\left[(\mu + \sigma\mu_T)\frac{\partial \omega}{\partial x_j}\right] \tag{5}$$

The empirical closure coefficients for the 1988 model are

$$\alpha = 5/9 \qquad \beta = 3/40 \qquad \beta^* = 9/100 \qquad \sigma = \sigma^* = 1/2 \tag{6}$$

This model was chosen because of its good capability in predicting separation and in dealing with adverse pressure gradients and separated flows when compared to other two-equation models.[4,5]

The numerical solver used in this study is AeroSoft's structured flow solver GASP Version 4.0. GASP was selected because it is a mature program with a proven reliability record in simulations of turbulent flows,[6] vortical flows,[7] jets,[8] and shock-vortex interaction and jet-interaction flows.[9] GASP solves the integral form of the time-dependent RANS equations in three dimensions. For a full description of GASP and its capabilities, see Refs. 10 and 11.

The solution was driven to a steady state using the implicit Gauss–Seidel scheme. The inviscid fluxes were computed in the three dimensions using the flux-vector splitting of Roe and had third-order spatial upwind biased accuracy with the min-mod limiter. The viscous terms are discretized using a standard second-order-accurate central differencing scheme. An exception to this flux combination was the replacement in only one computational direction of the Roe flux with the Van Leer flux leaving all of the other parameters unchanged to avoid the "carbuncle effect."[12]

Grid Selection

Several jet-interaction calculations were run before the Virginia Tech experimental cases. The computational grids used in these calculations were developed in several consecutive stages. As calculations proceeded and a better understanding of the flowfield was obtained, the grid was adapted to better resolve the salient characteristics of the flow without drastically increasing the total number of cells. The final grid design that stemmed from this process is a combination of H-type and C-type grids that allows a near-optimal cell clustering near the injector. The grid size was dictated by the need to find a balance between the grid refinement and the time to converge a solution to a steady state. A typical grid is shown in Fig. 1.

All grids were created using GRIDGEN Version 13.3 (Ref. 13). Care was taken to ensure that the cells closest to the solid surface would lie below a y^+ of 1.0. One-dimensional hyperbolic tangent stretching[14] was used in all regions to distribute the cells along the grid connectors. The injector was simulated by cells on the surface of the flat plate with imposed pressure and velocity equal to the jet total conditions.

The grid was sequenced twice by eliminating every other cell in the three spatial directions. On average it would take 2090 total CPU hours using SGI Origin CPUs to converge a turbulent calculation on a 1.5-million-cell grid.

Computational Domain and Boundary Conditions

The computational domain for the flat plate with normal injection consisted of a six-sided box. The lower plane, that is, the plane defined by $y/d = 0.00$, corresponds to the solid surface of the flat plate. The no-slip condition ($u = v = w = 0.0$) is imposed on the flat plate along with $\partial p/\partial y = 0.0$ and the adiabatic wall condition $\partial T/\partial y = 0.0$. The surface is assumed to be smooth. The injector is cut in the surface of the flat plate. For each case investigated, the

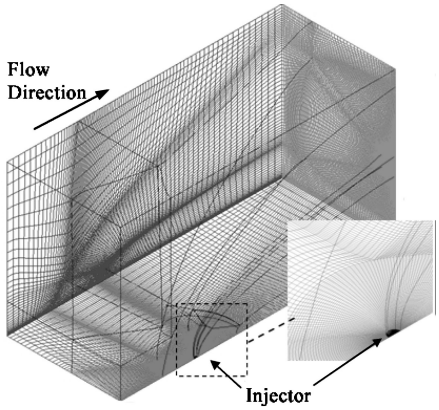

Fig. 1 Isometric view of the computational grid: 13 zones (mixed H- and C-type grids), 1,544,098 cells.

nozzle was choked, and the total conditions of the jet were known. Therefore, sonic conditions were applied at the cells simulating the jet ($Ma_J = 1.0, \rho_J = \rho^*, u_J = w_J = 0.0$ m/s, $v_J = v^*, p_J = p^*$). The jet was assumed to have a flat step profile, that is, no boundary layer in the nozzle was directly simulated. The area of the simulated jet is smaller than the real jet, and the ratio of the two areas is equal to the measured discharge coefficient Cd_J of the real nozzle. In this way, the viscous effects inside the nozzle were taken into consideration, and the mass flow of the simulated jet was the same as the real jet. The upstream surface was located 16 jet diameters ahead of the jet, based on data in the literature for the upstream extent of jet interaction flows. The flow upstream of the injector is supersonic, and a turbulent boundary layer is present. All of the dependent variables on the entry plane outside the boundary layer were assigned their respective freestream value. The freestream turbulence intensity (TI) was assumed to be 5% because no turbulence measurements were available. The entry boundary-layer thickness δ was obtained from the Schlieren pictures of the tunnel flow. The turbulent velocity boundary-layer profile was then assumed to follow the relationship

$$U/U_e = (y/\delta)^{\frac{1}{7}} \tag{7}$$

The symmetry plane is represented by the x–y plane. The symmetry boundary condition is taken such that the primitive variables are reflected across this plane with the exception of one velocity component, which is reversed. The three remaining sides of the computational domain (the exit plane, the top surface, and the longitudinal plane opposite the symmetry plane) do not represent any physical surface. The exit plane was located 48 jet diameters behind the jet, the top surface was 48 jet diameters above the wall, and the side surface was 24 jet diameters from the plane of symmetry. These choices were based on data in the literature for the extent of jet interaction flows. The top surface and the side wall of the wind tunnels were assumed to be distant enough from the injector not to interfere with the flowfield of interest. Therefore, a first-order extrapolation boundary condition was applied to these surfaces. The iterative convergence of the calculations was determined by checking the variation over time of several flow parameters. Convergence was declared when the variation of the normal force, axial force, and pitching moment over time was negligible. A complete description of the computations can be found in Ref. 15.

Note that according to the coordinate axis used to define the computational domain in this study, a negative pitching moment about the center of the primary jet indicates a nose-down moment.

Setup of the Experiments

Wind Tunnel

Experiments were performed at $M = 4.0$ by using the 23×23 cm Virginia Tech Supersonic Wind Tunnel with a nominal stagnation pressure of 20.5 atm (300 psi) and a stagnation temperature of 300 K. Tunnel control system uses a hydraulically actuated regulating, 30.5-cm-diam valve and a quick-opening butterfly valve. Most of the wind-tunnel operation and data acquisition are controlled by LabView.

Injectant Supply System

The air supply located outside provides air to the jet plenum using a piping system. The air bottles are connected through a manifold to a hand-operated on/off valve. This valve initiated flow into a high-pressure, high-mass-flow dome regulator, which stepped down the pressure from 150 atm (2200 psi). The air through the dome regulator passed several valves and reached the circular sonic jet nozzle. The nominal jet stagnation pressure is 38 atm (556 psi) leading to a jet stagnation to tunnel stagnation pressure ratio of 532. The jet mass flow rate was measured with a venturi flowmeter.

Schlieren System

A spherical mirror of 30-cm diam with a focal length of 200 cm was used. The light source system consists of a 1.2-μs Strobotac, a convex lens, and an adjustable light slit. Polaroid 4×5 ISO 3000 film is used for the schlieren images.

PSP System

PSP was used to analyze the flowfield around the side jet because this method provides continuous, spatial pressure data. The PSP technique is based on oxygen-quenched photoluminescence stimulated by the absorption of light. ISSI, Inc., brand Uni-FIB PSP was used. The paint contained two parts: an oxygen permeable flouroacrylic copolymer (FIB) binder and a fluorinated platinum porphyrin meso-tetra-pentaflourophenyl porphrine [Pt(TfPP)] oxygen-sensitive probe molecule. The PSP was applied using an airbrush sprayer. The temperature sensitivity was 0.6%/°C. The paint was illuminated with two blue (464-nm) light-emitting diode (LED) light sources (0.25 W each). The luminescence output (650 nm) was acquired with a 16-bit charge-coupled-device (CCD) camera. The paint calibration stemmed from the Stern–Volmer relationship, where the pressure was expressed as a function of I_{ref}/I. As suggested by the manufacturer, the calibration data were fit with a second-order polynomial. An average background image was subtracted from both the averaged wind-off and averaged wind-on images. The ratio of the subtracted wind-off I_{ref} and the subtracted wind-on images I was then converted into the surface pressure. The PSP uncertainty estimate included system (calibration and camera) as provided by the manufacturer (2.0% of the full-scale range) and surface temperature. The surface temperature was known to approximately ±5K, and the temperature sensitivity was 0.6%/K. Hence, the overall L_2 norm was computed as 3.6% of the full scale range.

The pictures were treated with ISSI OMS v.2.5 software. The photos are calibrated with the pressure tap measurements to produce a continuous picture of the pressure over the surface.

Test Model

The test model consisted of a plate forming the lower wall of the test section with a ramp that can be attached to it (Fig. 2). The brass plate is approximately 30 cm long by 23 cm wide. The plate also has a nozzle for the 0.48-cm-diam jet. The ramp is also constructed from brass, and six pressure taps are on the ramp. The ramp can be attached and detached from the plate.

Cubbison et al.[16] showed the surface-pressure distribution for a main jet at Mach 3, and the pressure tap locations were selected by referring to Cubbison's results. Figure 3 shows an overlay of

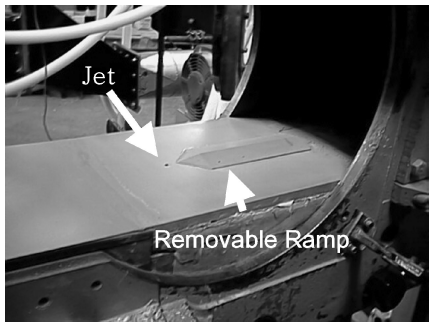

Fig. 2 Setup of ramp model in test section. (Flow is from left to right; tunnel doors are opened.)

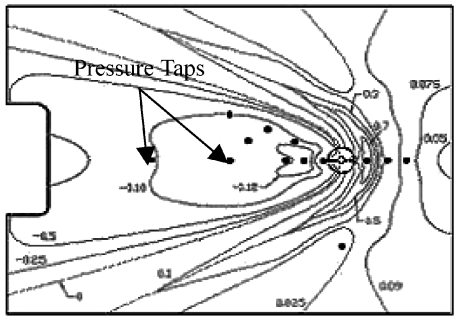

Fig. 3 Test plate layout with pressure coefficient overlay from Cubbison et al.[16]

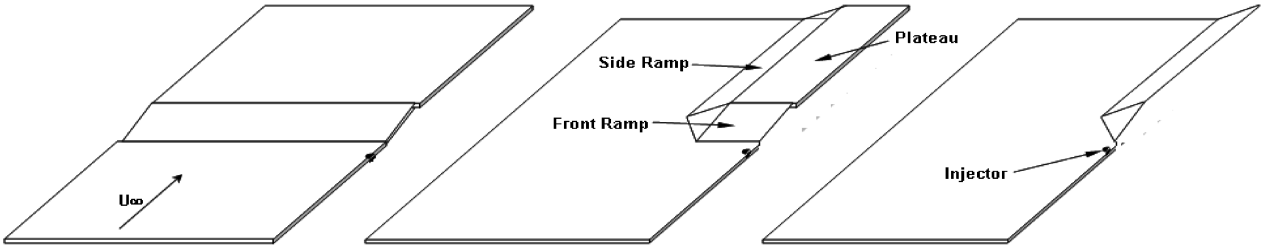

a) Two-dimensional ramp **b) Three-dimensional ramp, full plateau** **c) Three-dimensional ramp, no plateau**

Fig. 4 Three basic ramp designs that were tested in the computational parametric study.

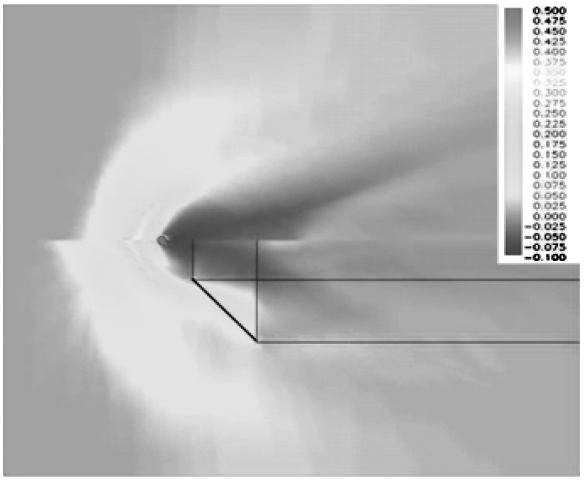

Fig. 5 Comparison of predicted C_p between cases with jet-plus-ramp (bottom half) and jet-only (top half) (ramp with wide plateau).

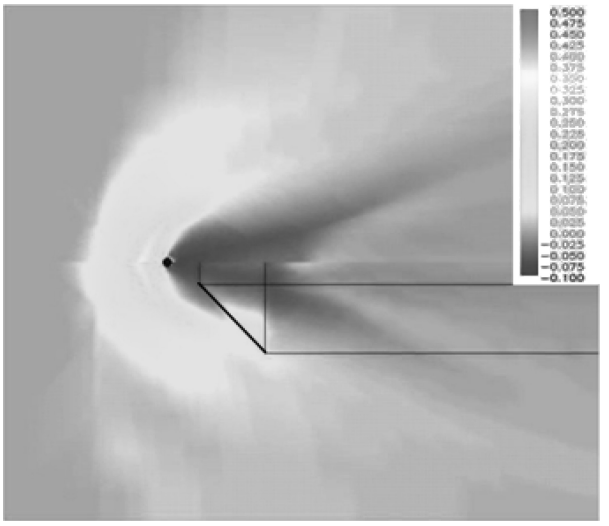

Fig. 6 Comparison of predicted C_p between cases with jet-plus-ramp (bottom half) and jet-only (top half) (ramp with narrow plateau).

Cubbison's results and the 12 pressure tap positions on the plate without the ramp. Before the start of the experimental study, the shape and dimensions of the ramp were optimized through a computational parametric study aimed at guiding the design of the ramp by optimizing its shape within the design constraints, so that the best performance could be obtained. By best performance we mean the optimal combination of a decrease in nose-down pitching moment, an increase (or no decrease) in normal force and a decrease/no effect in the drag. A numerical study was chosen over an experimental study because of its inherent lower costs and faster turnaround times. In addition, a numerical solution provides detailed information about the whole flowfield, which is a highly desirable feature when designing for optimum performance. Experiments, on the other hand, usually provide data at discrete points in the flowfield. The parametric study comprised of three basic ramp shapes as shown in Fig. 4. Initially, a set of two-dimensional ramps was tested so as to isolate the effects on the performance of three main parameters, nominally the ramp height, the angle of the inclined plane, and the distance of the ramp aft of the injector (Fig. 4a). Once these two parameters had been fixed according to the CFD results, a three-dimensional ramp was studied in order to optimize the width of the ramp plateau (Fig. 4b). The optimized ramp configuration, shown in Fig. 4c, was the final product of this iterative design loop. Note that the final ramp design did not feature any plateau.

Figures 5 and 6 show two of the predicted C_p plots on the surface of the flat plate and the ramp produced during the parametric study. The top part of each figure represents the case with injection but without a ramp. The bottom part of each figure shows the C_p map corresponding to the ramp case. The ramp footprint is visible as black solid lines. Figure 5 shows the results for a three-dimensional ramp with a relatively wide plateau. Note the higher pressures aft of the injector in the ramp case (bottom) as compared to the no-ramp case. The inclined plane of the ramp shows a large region of high pressure. Although this trend is desirable because it increases the normal force and it reduces the nose-down pitching moment, it also considerably increases the drag of the configuration.

Figure 6 shows a similar ramp configuration, but with a narrower plateau. In this case, the integration of the aerodynamic forces produced similar trends as those noted in Fig. 5, but with less drag penalty because the ramp cross section is smaller.

The final ramp design is detailed in Fig. 7. Six pressure taps are located on the ramp. The ramp can be attached and detached on the same plate used for the jet-only cases.

Results and Discussion

Flow Visualization

The experiments were run at a freestream Mach number 4 and for two cases, namely, jet-only and jet-plus-ramp cases. The results are compared for both cases. To determine the flow structure and compare with CFD data, flow-visualization experiments were conducted.

The upper schlieren picture of Fig. 8 is for the jet-only case, and the lower picture is the jet-plus-ramp case. Each picture shows the barrel shock, Mach disk, and lambda shock, which is created by the separated region upstream of the jet.

The case of the jet with the ramp shows a different shock shape from the jet-only case. It suggests that a complicated interaction occurred between the ramp and the shock. These effects are shown also in the pressure data.

Surface-Pressure Results

Figure 9 shows the measured and predicted pressure coefficient along the centerline for the jet-only case. The PSP results are shown as a dashed line, and the square symbols are the pressure tap results. The PSP results agree with the pressure tap results, and the CFD results correspond with pressure tap results except within 0.04–0.08 m

region. In the real, experimental situation, the pressure recovery to the freestream value occurs later than the CFD predicts.

In Fig. 10, there are only four pressure taps along the centerline in the jet-plus-ramp case as a result of the presence of the ramp itself. In this case, all data correspond quite well with each other, except that the high-pressure peak ahead of the jet seems overpredicted by the CFD. It is possible that the PSP fails to capture this sharp peak. These two graphs tell in more detail the merits of the jet-plus-ramp case than the visualization results. Along the centerline, the magnitude of the high pressure upstream of the jet is higher than in the jet-only case, and the low pressure downstream of jet is also raised. This fact is demonstrated well by the pressure tap data comparison in Fig. 11.

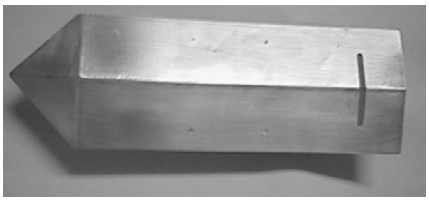

a) Plan view of ramp model

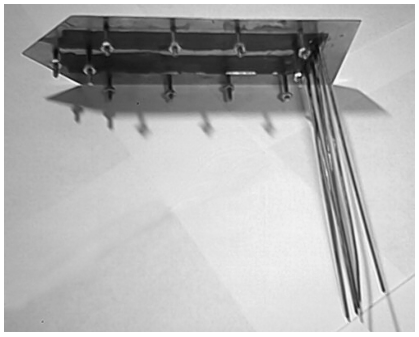

b) Bottom view of ramp model

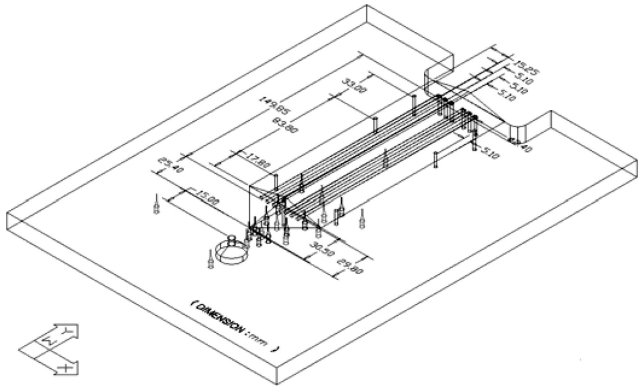

c) Details of ramp design

Fig. 7 Photos of ramp model.

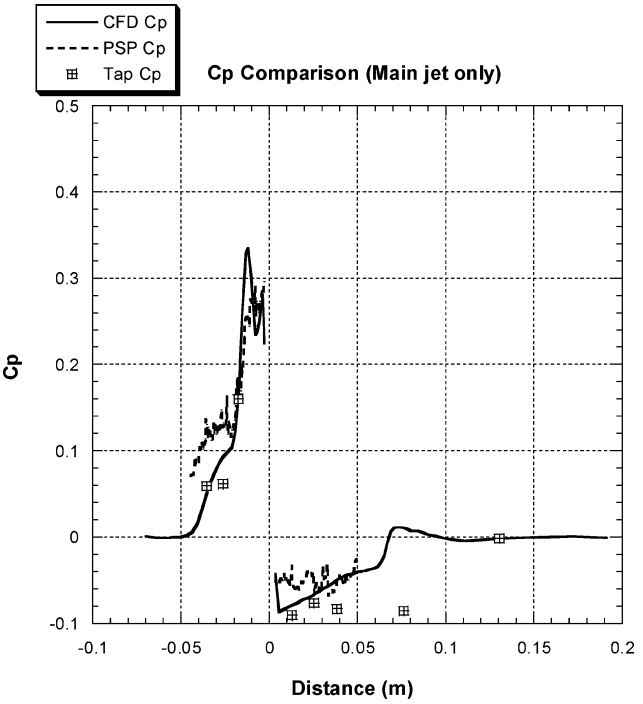

Fig. 9 C_p plotted along the centerline for jet-only case.

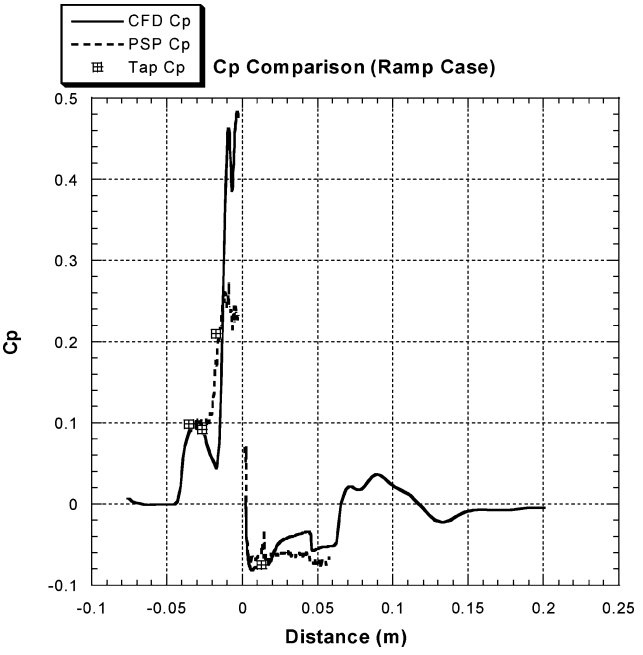

Fig. 10 C_p plotted along the centerline for the jet-plus-ramp case.

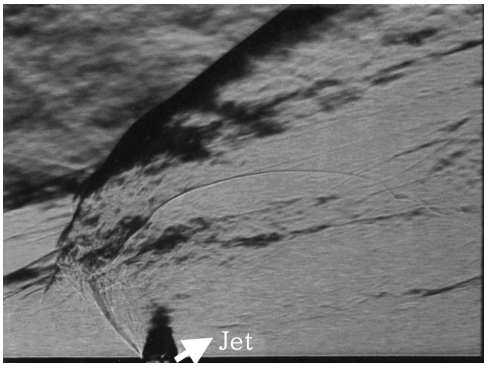

a) Jet-only case

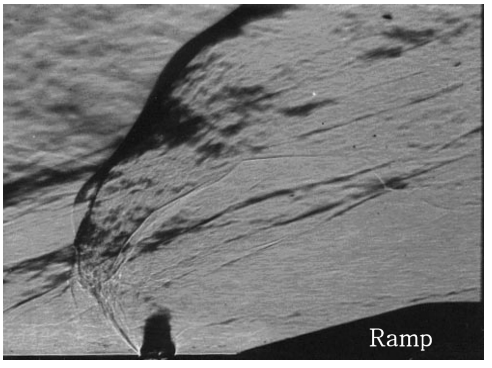

b) Jet-plus-ramp case

Fig. 8 Schlieren photographs of jet-only and jet-plus-ramp cases. Main flow is from left to right.

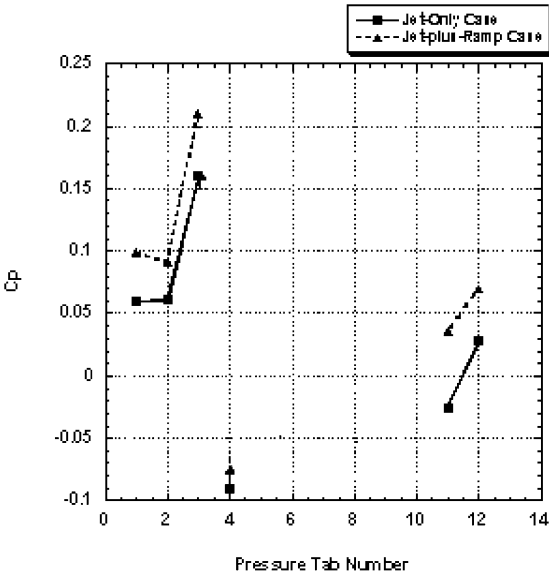

Fig. 11 Comparison of measured C_p between jet-plus-ramp case and jet-only case.

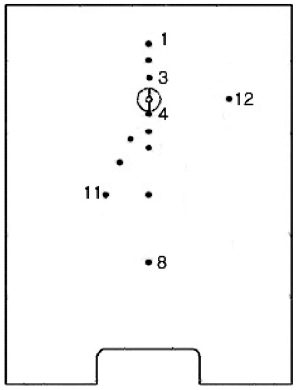

a) Jet-only case

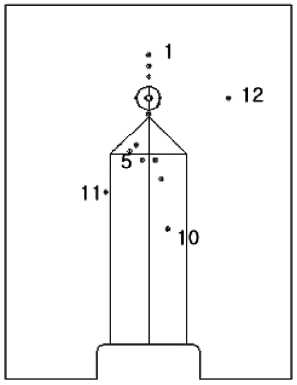

b) Jet-plus-ramp case

Fig. 12 Pressure tap locations.

Each pressure tap has a number for easy understanding. Figure 12 shows the number of pressure taps.

For the jet-only case, Fig. 9 shows only the pressure coefficient along the centerline, but Fig. 13 helps in understanding the structure of the flowfield over the whole surface. The high-pressure region of the PSP results is wider than the CFD result, and the separation shock region is also wider.

For the jet-plus-ramp case results in Fig. 14, the high-pressure region of the PSP results are also wider than CFD, but the intensity of the shock in the CFD results is stronger than the PSP.

Figure 15 shows the effects of the ramp directly. The strength of the shock is reduced upstream of the jet in the ramp case, and

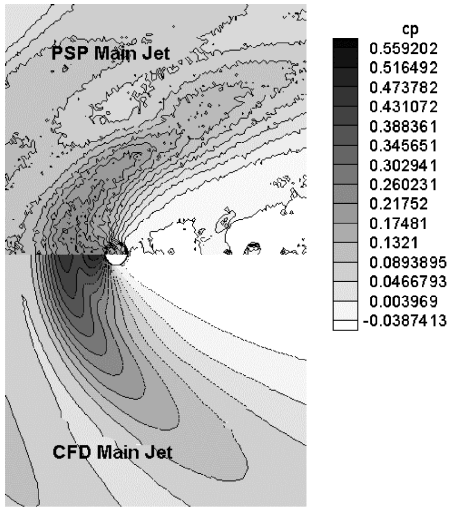

Fig. 13 Comparison of experimental and computational C_p results for the jet-only case.

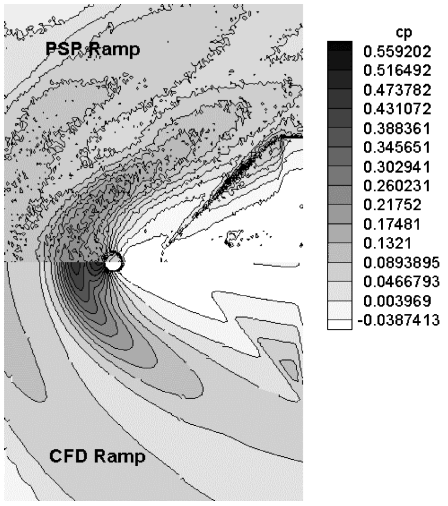

Fig. 14 Comparison of experimental and computational C_p results for the jet-plus-ramp case.

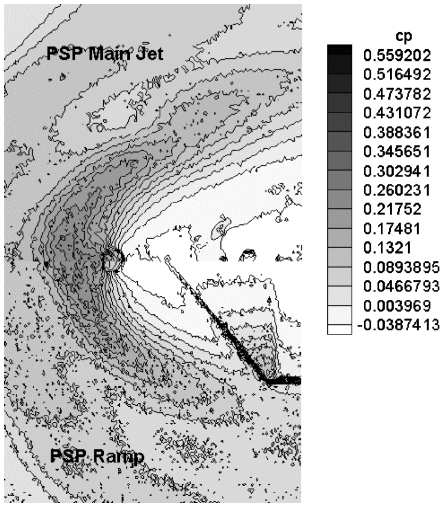

Fig. 15 Comparison of experimental C_p results between the jet-only case (top half) and the jet-plus-ramp case (bottom half).

Table 1 Normal force and moment coefficient comparison

Description	C_F	% Change	C_M	% Change
Jet-only (CFD)	0.01293	——	−0.005793	——
Jet-only (PSP)	0.04874	——	−0.002600	——
Jet-plus-ramp (CFD)	0.04804	−1.4	−0.000759	−70.8
Jet-plus-ramp (PSP)	0.04805	−1.4	−0.000895	−65.6

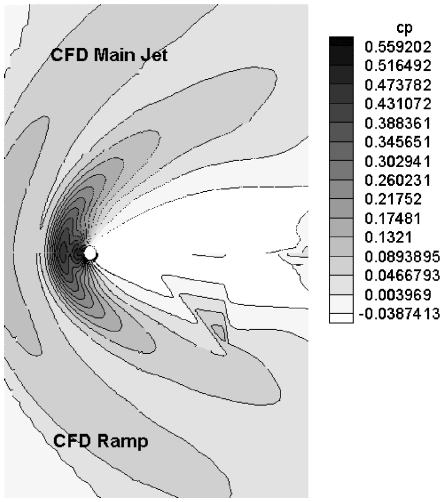

Fig. 16 Comparison of CFD C_p results between the jet-only case (top half) and the jet-plus-ramp (bottom half).

also the low-pressure region downstream of the jet is smaller than in the jet-only case. Figure 16 shows the same tendency in the CFD predictions.

If only the near-jet region on the plate is considered, the unwanted nose-down moment will be reduced.

Table 1 shows the summary of the force and the moment coefficient results. The area used for the integration was the 5.5×10^{-3} m^2 area covered by the PSP results. The moment center was taken as a center of jet. The thrust from the main jet was not included. As shown in Table 1, the moment for the ramp case was dramatically reduced without a force decrease.

Summary

In this study, the effect of a ramp located downstream of a side jet in supersonic crossflow was examined experimentally and numerically. PSP was used for measurement of the surface-pressure field for quantitative analysis, and schlieren photos were used for qualitative analysis.

The main results were as follows:

1) The schlieren photos show the flow structure such as barrel shock, Mach disk, and bow shock. They also showed different shock shapes between the jet-only case and the jet-plus-ramp case.

2) For the jet-only case, the PSP data overpredicted a little compared to the pressure tap results but compared well with CFD results.

3) For jet-plus-ramp case, the PSP data, pressure tap results, and CFD results predicted almost the same pressure except just in front of the main jet, where the CFD results showed much higher peak values than the PSP data.

4) The force and moment coefficient were calculated. Force coefficients of both cases did not change, but the generally undesirable nose-down moment coefficient of jet-plus-ramp case was reduced by almost 70% with respect to the jet-only case.

5) Based on these results, the concept of a ramp(perhaps retractable) located downstream of a control jet appears attractive and should be subjected to future study.

Acknowledgments

The first author acknowledges the support of the Agency for Defense Development through Contract ADD-01-3-1. The authors thank Reece Neel at AeroSoft, Inc., for helping to run GASP.

References

[1]Jacobsen, L., Gallimore, S., Schetz, J., and O'Brien, W., "An Improved Aerodynamic Ramp Injector in Supersonic Flow," AIAA Paper 2001-0518, Jan. 2001.

[2]Viti, V., Schetz, J., and Neel, R., "Numerical Studies of the Jet Interaction Flowfield with a Main Jet and an Array of Smaller Jets," International Congress of Aeronautical Sciences, Paper 2002-4.7.1, Sept. 2002.

[3]Wilcox, D. C., *Turbulence Modeling for CFD*, 2nd ed., DCW Industries, Inc., La Cañada, CA, 1998, Chap. 4.

[4]Payne, J. L., Roy, C. J., and Beresh, S. J., "A Comparison of Turbulence Models for a Supersonic Jet in Transonic Cross Flow," AIAA Paper 2001-1048, Jan. 2001.

[5]Wilcox, D. C., "Comparison of Two-Equation Turbulence Models for Boundary Layers with Pressure Gradient," *AIAA Journal*, Vol. 38, No. 8, 1993, pp. 1414–1421.

[6]Roger, R. P., and Chan, S. C., "Parameters Affecting Penetration of a Single Jet into a Supersonic Crossflow: A CFD Study—II," AIAA Paper 98-0425, Jan. 1998.

[7]Nedungadi, A., and Lewis, M. J., "A Numerical Study of Fuel Mixing Enhancement Using Oblique Shock/Vortex Interactions," AIAA Paper 96-2920, Feb. 1997.

[8]Hsieh, T., "Analysis of the Scaling Effects for Missile Configuration with Lateral Thruster," AIAA Paper 99-0810, Jan. 1999.

[9]McDaniel, J., Glass, C., Staack, D., and Miller, C., "Experimental and Computational Comparison of an Underexpanded Jet Flowfield," AIAA Paper 2002-0305, Jan. 2002.

[10]*GASP 3.2 User Manual*, AeroSoft, Inc., Blacksburg, VA, 1997.

[11]*GASP 4.0 User Manual*, AeroSoft, Inc., Blacksburg, VA, 2001.

[12]Peery, K. M., and Imlay, S. T., "Blunt-Body Flow Simulations," AIAA Paper 88-2904, July 1988.

[13]*GRIDGEN Version 13.3 User Manual*, Pointwise, Inc., Bedford, TX, 1999.

[14]Vinokur, M., "On One-Dimensional Stretching Functions for Finite Difference Calculations," *Journal of Computational Physics*, Vol. 50, No. 3, 1983, pp. 215–234.

[15]Viti, V., "Numerical Studies of the Jet Interaction Flowfield with a Main Jet and an Array of Smaller Jets," Ph.D. Dissertation, Dept. of Aerospace and Ocean Engineering, Virginia Polytechnic Inst. and State Univ., Blacksburg, VA, Sept. 2002.

[16]Cubbison, R. W., Anderson, B. H., and Ward, J. J., "Surface Pressure Distributions with a Sonic Jet Normal to Adjacent Flat Surfaces at Mach 2.92 to 6.4," NASA TN D-580, 1961.

W. Williamson
Associate Editor